Wide field continuous wave reflectance optical topography including a clear layer on top of the diffusive surface.

N. A. Carbone, D. I. Iriarte, and J. A. Pomarico.
CIFICEN (UNCPBA - CONICET - CICBA)
Pinto 399 - B7000GHG - Tandil
ARGENTINA
juanp@exa.unicen.edu.ar

Abstract:

This work considers some experimental details which complement the results of a previous paper from 2014 by Carbone *et* al. [Biomed. Opt. Express, 5, 1336 (2014)] concerning with wide field Near Infrared Continuous Wave (CW) diffuse reflectance optical mammography. Different from the case of phantoms, clinical applications requires some transparent interface between the breast and the camera. This interface provides the necessary flat surface to be imaged by the camera. We present an experimental study which compares the performance of the method when such an interface is present, to the case of the exposed phantom's surface presented by Carbone et al. Several index matching materials are also included in the study and a validation using Monte Carlo is presented.

Keywords: Turbid Media, Imaging, Diffuse Reflectance, NIRS.

1. Introduction

For the last decades scientists have been interested in the propagation of near infrared (NIR) light in turbid media because this non invasive radiation has proved several potential applications, being optical imaging of biological tissues of utmost importance. As it is well known, diverse approaches and geometries are possible; briefly, diffuse transmission and reflection are the most usual geometries, and sources can be either continuous (CW), pulsed or modulated. Many biomedical applications have been developed, from bed side monitoring of cerebral blood flow,[1,2] to detection of breast cancer [3], to mention but a few. Most techniques rely on contrast due to different concentrations of the natural chromophores, such as oxy- and deoxy-hemoglobins. However, the diffusive nature of photon migration in tissues strongly degrades spatial information, making, in general, functional imaging,[4–6] easier than structural imaging [7-9].

In particular, diffuse reflectance from optically turbid tissue has been exploited for near infrared (NIR) spectroscopy and NIR diffuse optical imaging (DOI), relevant for several applications in biomedical optics [10-13].

Imaging and characterization of embedded lesions in turbid media means discrimination of signal changes due to absorption and/or scattering in the presence of these lesions in comparison to signals when no lesions are present. Relatively sophisticated approaches allowing for that employ either spatially and/or temporally modulated light sources together with photon detection schemes of appropriate resolution [14,15]. Moreover, most of these techniques require scanning the region of interest, since they only allow imaging of small areas. Alternatively, wide-field diffuse optical imaging approaches employ discrete multi-distance source-detector separations or structured illumination and allow noncontact imaging of relatively large areas [16-21].

In a recent publication, Carbone *et al.*[22] demonstrated a technique for non-contact wide-field continuous wave (CW) imaging of lesions based on spatial point spread function measurement employing a CCD sensor in the diffuse reflection geometry. The approach described in that paper, could be useful for optical mammography avoiding breast compressions, typical for both, X-Ray mammography and optical approaches using transmission geometries, and thus allowing a more comfortable situation for patients. Briefly described, in that contribution from Carbone et al., several images of the accesible surface of a turbid medium with inclusions are taken. The average of all these images is used as a normalization background for each individual image, making evident the presence of the inclusions. In that paper, the limits of detection were theoretically explored as a function of several parameters, such as the intrinsic absorption contrast, the inclusion's depth and the inclusion's size. Additionally, an experiment on phantoms was presented, showing the viability of the approach. In the phantom experiment presented there, the exposed surface of the solid phantom was flat. Moreover, the surface of the phantom was in direct contact with air, and no other medium was placed between the phantom and the camera. However, this is not the case if a real measurement is to be done on human breasts. To provide a plane surface, some additional interface needs to be placed between the breast (resting on it) and the camera. A possible real clinical situation, sketched in Figure 1, could be a patient laying decubito prono with the breast compressed against a transparent flat surface by the natural body weight.

With that in mind, we studied the effect of a clear layer on top of a diffusive surface for the case of CW reflectance imaging as proposed by Carbone *et* al. In particular, we are interested in possible changes in the detectability of a lesion, that is, how contrast is modified by the presence of this clear layer.

The aim of this work was to investigate the effect of clear layers interfaces and index matching materials placed between the phantom and the camera, on the contrast of the detected inhomogeneity emulating the lesion. To this end, we performed a series of experiments and simulations to determine the best combination of layer and index matching material that leads to the minimum contrast degradation.

The paper is organized in the following way: in the next section we describe the rationale of the approach. Next, the experiments as well as the materials used are presented. Then we present the most important results, and in the final section we summarize the main conclusions of the work.

2. Rationale

To detect the inclusion and determine the contrast of the resulting image we used the method described in detail in by Carbone *et* al. Thus we summarize here only the main steps. First we proceed considering no clear layer on top of the diffusive surface. Information is acquired by imaging the accessible face of the scattering medium by a CCD camera, resulting in a series of *2D* pictures, $I_j(x,y), \; j = 1,2,...,N$, of the light being diffusely reflected. Each image was recorded for a different position of the phantom relative to the camera. This was achieved by rotating the phantom in front of the camera by an angle α_j, with center of rotation coincident with the optical axis. A sketch of the situation is depicted in Figure 2. To make the inclusion visible, each image is normalized by a background, $I_0(x,y)$.

Ideally this background can be taken as the same medium but without inclusion., but this can not be implemented in practical cases. Instead, the desired background was obtained by the average of all images, that is

$$I_0(x,y) = \frac{1}{N} \sum_{j=1}^{N} I_j(x,y)$$

Each normalized image was thus

$$I_j^N(x,y) = I_j(x,y) / I_0(x,y)$$

Now we have to consider the situation when a clear layer is present on top of the diffusive surface. For the case of Time Resolved (TR) measurements, the problem concerning with the Distributions of Times of Flight (DTOFs) in the presence of a clear layer, has been addressed by Del Bianco et al.[23], for both, diffuse transmittance and reflectance. That work demonstrated that the DTOF for diffuse transmittance is barely affected by clear layers up to several mm thick. However, for diffuse reflectance, the DTOFs are considerably distorted by the clear layer, especially if its thickness is larger than 2mm and for source - detector distances $\rho \approx 3\ cm$; please refer to figures 3 and 4 in the paper by Del Bianco *et al*. Of course, that is of crucial importance if the optical properties are to be retrieved from the corresponding DTOFs. However, if CW is used, and only detection of the inclusion is of concern, these differences are not of great significance, as we show in the following. In fact, considering a single pixel, integration of a temporal reflectance pulse, *R(t),* which represents the intensity in the CW approach, makes the temporal distribution of photons irrelevant. That is, the integrated pulse with a clear layer on top differs from the integrated pulse without clear layer at most in a scale factor, and thus we can write:

$$\int R_{Inc}^{CL}(t)\ dt = \kappa \ \int R_{Inc}(t)\ dt\ ,$$

being $\int R_{Inc}^{CL}(t)\ dt$ the integrated reflectance in the presence of the clear layer with

inclusion, $\int R_{Inc}(t)\ dt$ the integrated reflectance without the clear layer and with the

inclusion and κ a factor depending on the thickness of the clear layer and on the source – detector distance, ρ. In an equivalent way, if no inclusion is present, it holds

$$\int R^{CL}(t)\ dt = \kappa \ \int R(t)\ dt$$

.

Since the integrated reflectance of the phantom with clear layer is proportional to the integrated reflectance of the phantom without the clear layer, the normalization procedure (division) explained above will cancel out or minimize the effects of the layer on top of the phantom. As a consequence, the approach is expected to work properly even in the presence of a clear layer. However contrast modifications may occur, and determining them was the goal of this work.

3. Materials and methods

3.1. Phantom Experiments

To perform the experiments we used a solid phantom with an absorbing inclusion. The phantom consists of a cylinder of *13 cm* in diameter and is *4.3 cm* thick. It was made of epoxy resin with TiO2 as the scattering agent and toner powder as an added absorber. Their optical properties, measured at $830nm$ were: $\mu_a^0 = 0.11\ cm^{-1}$ for the absorption coefficient and $\mu_s'^0 = 10.6\ cm^{-1}$ for the reduced scattering coefficient. This phantom contained a spherical inclusion, made of the same type of epoxy resin, and it had a diameter of 1 cm and optical properties at the same wavelength as the host given by $\mu_a^{Inc} = 0.23\ cm^{-1}$ for the absorption coefficient and $\mu_s'^{Inc} = 11.8\ cm^{-1}$. Thus, the inclusion has approximately the same scattering coefficient as the bulk, and nearly twice its absorption. Please note, that the reduced scattering coefficient of the inclusion is not strictly the same as that of the bulk, but about 11% higher. This contributes to increase the extinction coefficient, and thus the effect of the scattering perturbation sums up to the effect of the absorption perturbation (i.e. both decrease the detected photons). The geometrical center of the inclusion was placed at *1.2 cm* depth and at *3 cm* from the cylinder longitudinal axis (see Figure 2). For this work we took 36 images ($N = 36$), each consisting of 768×512 pixels, one every 10 degrees. Figure 3 shows an actual picture of the surface of the phantom with the geometrical details superimposed. The phantom is illuminated by a *10 mW, CW, 830 nm* collimated diode laser. In Figure 3, the laser is identified by the capital letter *L* and the inclusion by *I*. Note that for different angular positions of the inclusion (α_j) the distance *d* from the laser to the inclusion is also different.

For the proposed study we used four different materials on top of the phantom, namely glass, ground glass, transparent plastic (Polymethyl methacrylate: PMMA) and white PMMA; all of them consisted of a $13\ cm \times 13\ cm$ sheet having a thickness of *0.2 cm*. Between them and the phantom a thin layer of some index matching material (IM) was used to improve optical coupling between the phantom and the interface sheet. As

possible IM we tested milk, a transparent gel (used for medical ultrasound diagnostics) and a commercial body cream, Nivea® (www.nivea.com).

To evaluate the contrast, we took a *1D* profile, $P_j(\xi)$, of the normalized image along the axis going through the illumination point and the center of the inclusion. Due to the absorbing nature of the sphere emulating the lesion, a dip in the profiles occured at those locations where the inclusion was detected. Additionally, since profiles were normalized, their maximum value was always one. Thus we will refer to the modulation depth (or just the modulation) of the profile as $M = 1 - P_j(\xi)_{min}$, being $P_j(\xi)_{min}$ the minimum value of $P_j(\xi)$. Larger modulation values correspond to better detectability of the inclusion. Since these profiles were noisy, an empirical, pulse shaped curve, $\tilde{P}_j(\xi)$, was fitted to the experimental data to obtain the minimum of the normalized profile, $\tilde{P}_j(\xi)_{min}$. We used this approach instead of any smoothing procedure, since smoothing can reduce the modulation. The analytical expression for the fitting function is given by $\tilde{P}_j(\xi) = 1 - A(\xi - \xi_0)^b \exp[-c(\xi - \xi_0)^2]$, being *A, b, c* and ξ_0 the fitting parameters.

The standard deviation of the experimental data was obtained from the fluctuations around the unit value of the profiles at distances far from the inclusion. A typical situation is plotted in Figure 4, showing both, the experimental and the fitted profile.

3.2. Monte Carlo simulations

As a validation of our results, we performed Monte Carlo (MC) simulations. It is a well known fact, that this kind of numerical simulation is very time consuming. To overcome this drawback, we used a self developed very fast MC algorithm for simulations in turbid media containing inhomogeneities that performs computing on the Graphics Processing Unit (GPU) instead of using the CPU, and is based on Compute Unified Device Architecture (CUDA). Due to the parallel processing capability of GPU, and depending on the graphics card used, calculation times can be reduced up to several orders of magnitude. Calculations were performed in the cluster from CeCAR (University of Buenos Aires, Argentina) which consists on 18 nodes each one having 2 AMD Opteron 6320 procesors, 64 GB of Ram and 2 Nvidia Tesla K20c GPUs.

In particular, the code we used, described by Carbone *et al*, was based on the open source code CUDAMCML for Multi- Layer turbid media[25], but allowing the possibility of including inhomogeneities. The code considers a multiple layer structure and inhomogeneities (one or more) can be located inside the desired layer. Our modified code treated the case of inhomogeneities embedded only in only one layer. Photons bundles were launched normal to the entrance face of a slab of thickness S and infinite lateral extension*,* and they were tracked until they were either completely absorbed, or exited the medium at the same face of the phantom within a defined detection area (diffuse reflection). Photons were collected on a grid at the entrance surface building up the diffuse reflectance image and Fresnel reflections were considered at every boundary involving refractive index changes. The inclusion was located at *1.2 cm* depth and at distances from the laser reproducing those given in Figure 3 for the different angular positions. The optical properties of the turbid layers and the inclusion were taken from those used for the phantom experiments. Absorption and scattering of the clear layer were considered null. For each situation, two diffuse reflectance images were generated, namely one with the inclusion inside the turbid medium and one without it. This last one provided the normalization background. The process followed in a similar way as for the phantom experiments by dividing each image obtained with the inclusion in place by the background and drawing normalized intensity profiles along the line connecting the illumination point with the center of the inclusion. Finally, the contrast was measured from these profiles. Results corresponding to MC simulations are presented in Figure 6 for the case of a glass clear layer and using the body cream as index matcher together with the results for the phantom experiments, showing good agreement.

4. Results and discussion

As already stated, the images were obtained by rotating the phantom in 10 degrees steps. A total of *36* images were recorded, each of then was normalized accordingly to Eq. and the corresponding profiles (in one dimension) were taken as described. Because of the increasing distance, *d*, between the illumination point and the inclusion, the inclusion is visible only for a few positions of the phantom which are relatively close to the point where laser impinges on the phantom`s surface. With reference to

Figure 3, these positions correspond to angles $\alpha_j = 0^\circ$ (the starting position), $\alpha_j = 10^\circ$

and $\alpha_j = 20^\circ$. Clearly, the images of the symmetrical positions ($\alpha_j = 340^\circ$ and

$\alpha_j = 350^\circ$) also produced a visible inclusion. The corresponding distances for these

angles are: $d^{0^\circ} = 1.75cm$, $d^{10^\circ} = 1.87cm$ and $d^{20^\circ} = 2.20cm$.

Not every combination of interface material-index matcher allowed detection of the inclusion. In fact, using a scattering material, such as ground glass or white PMMA strongly degraded contrast, independently of the distance from the inclusion to the illumination point (Figure 5). This can be explained by the fact that in this case, when white PMMA or a ground glass are used as top layers, which are diffussive themselves, this additional diffusive layer makes the inclusion to lie deeper, with the consequent loss in contrast (Carbone *et al* [22]). Thus, the case of white PMMA is considered only for comparison purposes. Because of this we present mainly the results corresponding to the transparent glass interface with different IM. Using transparent PMMA produced the same results as transparent glass.

On Table 1 we summarize the modulations resulting for the glass with different IM and

for the five positions corresponding to angles from 340° to 20° in 10° steps. The

modulations for the phantom without any interface are given as a reference. Clearly the best modulation was achieved when using the glass interface with the body cream as index matcher. The results shown in this table are also plotted in Figure 5. In this figure all values are normalized to the modulation corresponding to the minimum distance from the laser of the phantom without covering layer. From it, besides the observed good modulation of glass/body cream, we notice that the curve corresponding to the glass without IM has also a fairly good modulation, which is even better than that of the

glass with milk as IM. In all cases the position $\alpha_j = 0^\circ$ corresponds to the minimum

distance between the illumination point and the inclusion, resulting in the best modulation. Clearly if a diffusive medium is used as interface the modulation is drastically reduced; the case of PMMA is shown here. The lines joining the symbols are just a guide for the eye and they do not represent any fitting of the data.

As a comparison, MC simulations are presented in Figure 6 together with experimental results, showing the change in contrast relative to the phantom without cover layer. Simulations were carried on for a phantom with a *0,2 cm* thick glass layer with body

cream as index matcher. The thickness of this last one was considered to be *0.2 mm*, and their optical properties were measured separately, resulting $\mu_s^{\prime IM} = 36.8~cm^{-1}$ and $\mu_a^{IM} = 0.018~cm^{-1}$ The solid horizontal line in Figure 6 represents no change in contrast. The shown MC simulations agree fairly well with the corresponding experiments, indicating deviations of less than 1.5% percent.

5. Conclusions

In this work we presented an experimental study to complement the findings reported previously by Carbone *et al.*[22] where a phantom emulating a compressed breast was used without any interface between it and the camera. The most similar clinical situation would be a breast compressed by the body of the patient laying decubito prono on a flat transparent surface. Thus, this work used different materials as interface layers and several index matching materials to evaluate the performance of the method proposed by Carbone *et al.*[22] in situations close to the described clinical application for the case of optical mammography. The main conclusion is that a glass interface between the phantom emulating the patient's breast and the camera, with a commercial cosmetic body cream (Nivea®) as index matcher, is the best combination, since it reproduces the contrast of the detected inclusion without any loss with respect to the laboratory situation in which the flat surface of the phantom is imaged by the camera with no other medium between them.

References and links

1. A. Jelzow, H. Wabnitz, H. Obrig, R. Macdonald, J. Steinbrink, "Separation of indocyanine green boluses in the human brain and scalp based on time-resolved in-vivo fluorescence measurements", *J. Biomed. Opt*. **17** (5), 057003 (2012). doi:10.1117/1.JBO.17.5.057003.

2. Tuan Vo. Dinh, Biomedical Photonics Handbook, CRC Press (2003).

3. A. Pifferi, A. Torricelli, L. Spinelli, D. Contini, R. Cubedu, F. Martelli et al., "Time-resolved diffuse reflectance using small source-detector separation and fast single-photon counting", *Phys. Rev. Lett*. **100**, 138101 (2008).

4. G. Yu, T. Durduran, G. Lech , C. Zhou, B. Chance, E. R. Mohler , A. G. Yodh, "Time-dependent blood flow and oxygenation in human skeletal muscles measured with noninvasive near-infrared diffuse optical spectroscopies", *J. Biomed. Opt*. **10** (2), 024027 (2005).

5. J. D. Riley, F. Amyot, T. Pohida, R. Pursley, Y. Ardeshirpour, J. M. Kainerstorfer, L. Najafizadeh, V. Chernomordik, P. Smith, J. Smirniotopoulos, E. M. Wassermann and A. H. Grandjbakhche, "A hematoma detector - a practical application of instrumentalmotion as signal in near infra - red imaging", *Biomed. Opt. Exp*. **3** (1), 192 - 205 (2012).

6. E. M. Hillman. "Optical brain imaging in vivo: techniques and applications from animal to man", *J. Biomed. Opt*. **12** (5), 051402 (2007).

7. L. Spinelli, A. Torricelli. A. Pifferi, P. Taroni, G. M. Danesini and R. Cubeddu, "Bulk optical properties and tissue components in the female breast from multiwavelength time-resolved optical mammography", *J. Biomed. Opt*. **9** (6), 1137-1142 (2004).

8. D. Grosenick, H.Wabnitz, H. Rinneberg, K. T. Moesta and P. Schlag, "Development of a Time-Domain Optical Mammograph and First in vivo Applications", *Appl. Opt*. **38** (13) 2927 - 2943 (1999).

9. C. H Schmitz, D. P. Klemer, R. Hardin, M. S. Katz, Y. Pei, H. L. Graber, M. B. Levin, R. D. Levina, N. A. Franco, W. B. Solomon and R. L Barbour, "Design and implementation of dynamic near-infrared optical tomographic imaging instrumentation for simultaneous dual-breast measurements", *Appl. Opt*. **44** (11), 2140-2153 (2005).

10. B. J. Tromberg, N. Shah, R. Lanning, A. Cerussi, J. Espinoza, T. Pham, L. Svaasand, J. Butler, "Non-Invasive In Vivo characterization of Breast Tumor using Photon Migration Spectroscopy", *Neoplasia*. **2** (1), 26-40, (2000).

11. R. Choe, A. Corlu, K. Lee, T. Durduran, S. D. Konecky, M. Grosicka-Koptyra, S. R. Arridge, B. J. Czerniecki, D. L. Fraker, A. DeMichele, B. Chance, M. A. Rosen, and A. G. Yodh, "Diffuse optical tomography of breast cancer during neoadjuvant chemotherapy: A case study with comparison to MRI", *Med. Phys*. **32** (4), 1128-1139 (2005).

12. A. Cerussi, N. Shah, D. Hsiang, A. Durkin, J. Butler, and B. J. Tromberg, "In vivo absorption, scattering, and physiologic properties of 58 malignant breast tumors determined by broadband diffuse optical spectroscopy", *J. Biomed. Opt*. **11** (4), 044005 (2006) .

13. A. P. Gibson, J. C. Hebden and S. R. Arridge, "Recent advances in diffuse optical imaging", Phys. Med. Biol. 50 R1-R43, (2005). 14. D. Grosenick, A. Hagen, O. Steinkellner, A. Poellinger, S. Burock, P. Schlag, H. Rinneberg and R. Macdonald, "A multichannel time-domain scanning fluorescence mammograph: Performance assessment and first in vivo results", *Rev. Sci. Instrum*. **82** 024302 (2011).

15. V. Nziachristos, X. Ma, and B. Chance. "Time Correlated Single Photon Counting Imager for Simultaneous Magnetic Resonance and Near Infrared Mammography", *Rev. Sci. Instrum.* **69** 4221-4223 (1998).

16. T. Dierkes, D. Grosenick, T. Moesta, P. Schlag, H. Rinneberg, S. Arridge, "Reconstruction of optical properties of phantom and breast lesion in vivo from paraxial scanning data", *Phys. Med. Biol.* **50** (11), 2519-2542 (2005).

17. T. O´Sullivan, A. Cerussi, D. Cuccia and B. Tromberg, "Diffuse optical imaging using spatially and temporally modulated light", *J. Biomed. Opt.* **17** (7), 071311 (2012).

18. S. Gioux, A. Mazhar, D. J. Cuccia, A. J. Durkin, B. J. Tromberg, J. V. Frangioni, "Three-dimensional surface profile intensity correction for spatially modulated imaging", *J. of Biomed. Opt.* **14** (3), 034045 (2009).

19. A. Bassi, D. J. Cuccia, A. J. Durkin, and B. J. Tromberg, "Spatial shift of spatially modulated light projected on turbid media", *J. Opt. Soc. Am. A* **25** (11), 2833-2839 (2008).

20. S. Gioux, A. Mazhar, B. T. Lee, S. J. Lin, A. Tobias, D. J. Cuccia, A. Stockdale, R. Oketokoun et al. "First-in-human pilot study of a spatial frequency domain oxygenation imaging system", *J. Biomed. Opt.* **16** (8), 086015 (2011).

21. J. R. Weber, D. J. Cuccia, W. R. Johnson, G. H. Bearman, A. J. Durkin, M. Hsu, A. Lin, D. K. Binder, D.Wilson, and B. J. Tromberg, "Multispectral imaging of tissue absorption and scattering using spatial frequency domain imaging and a computed-tomography imaging spectrometer", *J. of Biomed. Opt.* **16** (1), 011015 (2011).

22. N. A. Carbone, G. R. Baez, H. A. García, M. V. Waks Serra, H. O. Di Rocco, D. I. Iriarte, J. A. Pomarico, D. Grosenick, and R. Macdonald, "Diffuse reflectance optical topography: location of inclusions in 3D and detectability limits", *Biomed. Opt. Express* **5** (5), 1336 - 1354, (2014).

23. S. Del Bianco, F. Martelli and G. Zaccanti, "Effect of a clear layer at the surface of a diffusive medium on measurements of transmittance and reflectance", *Opt. Express* **12** (22), 5510 - 5517, (2004).

24. N. A. Carbone, H. O. Di Rocco, D. I. Iriarte and J. A. Pomarico, " Solution of the direct problem in turbid media with inclusions using Monte Carlo simulations implemented in graphics processing units: new criterion for processing transmittance data", *J. of Biomed. Opt.* **15** (3), 035002 (2010).

25. E. Alerstam, T. Svensson, and S. Andersson-Engels, "Parallel computing with graphics processing units for high-speed Monte Carlo simulation of photon migration," *J. of Biomed. Opt.* **13** (6), 060504 (2008).

Figure 1

N. A. Carbone, D. I. Iriarte and J. A. Pomarico.

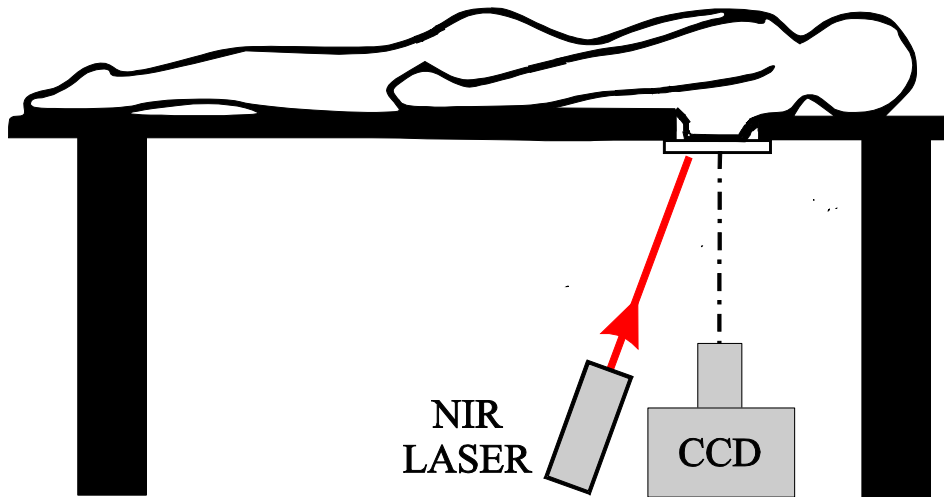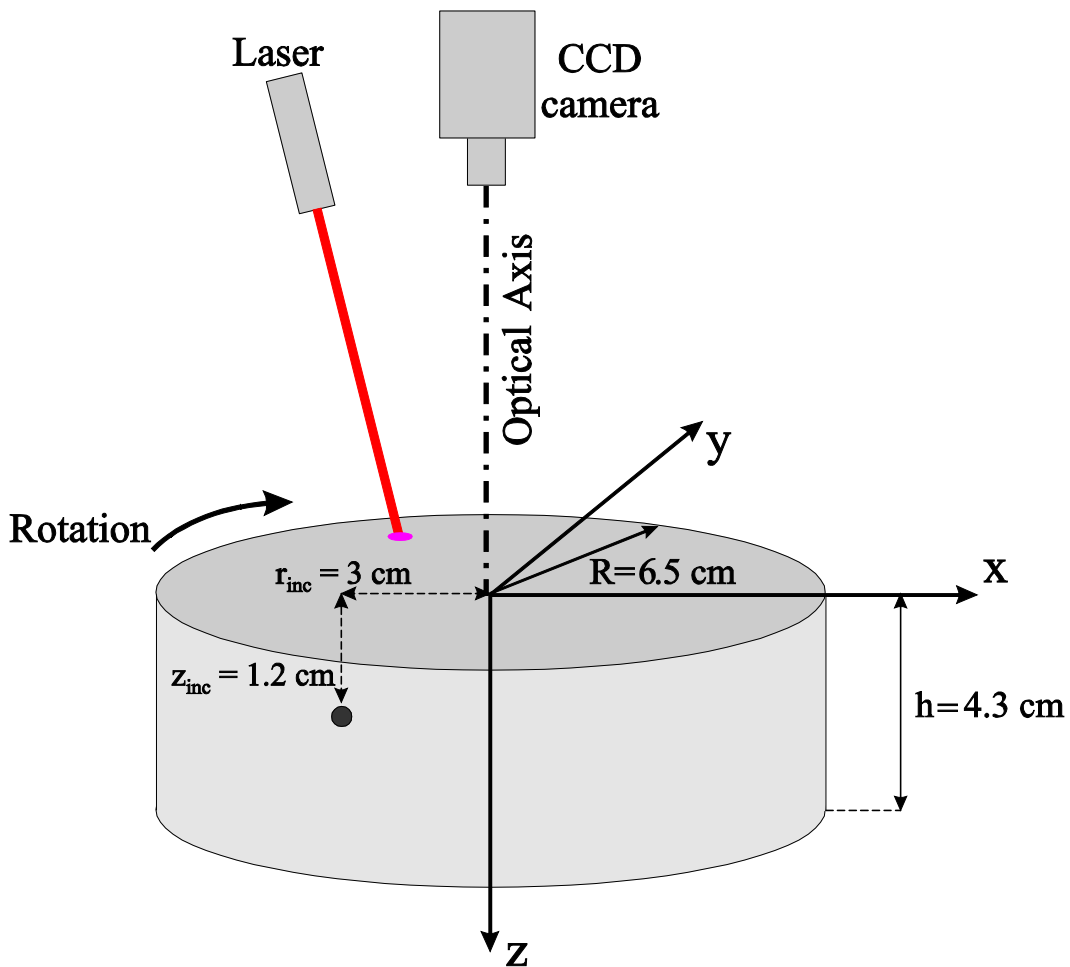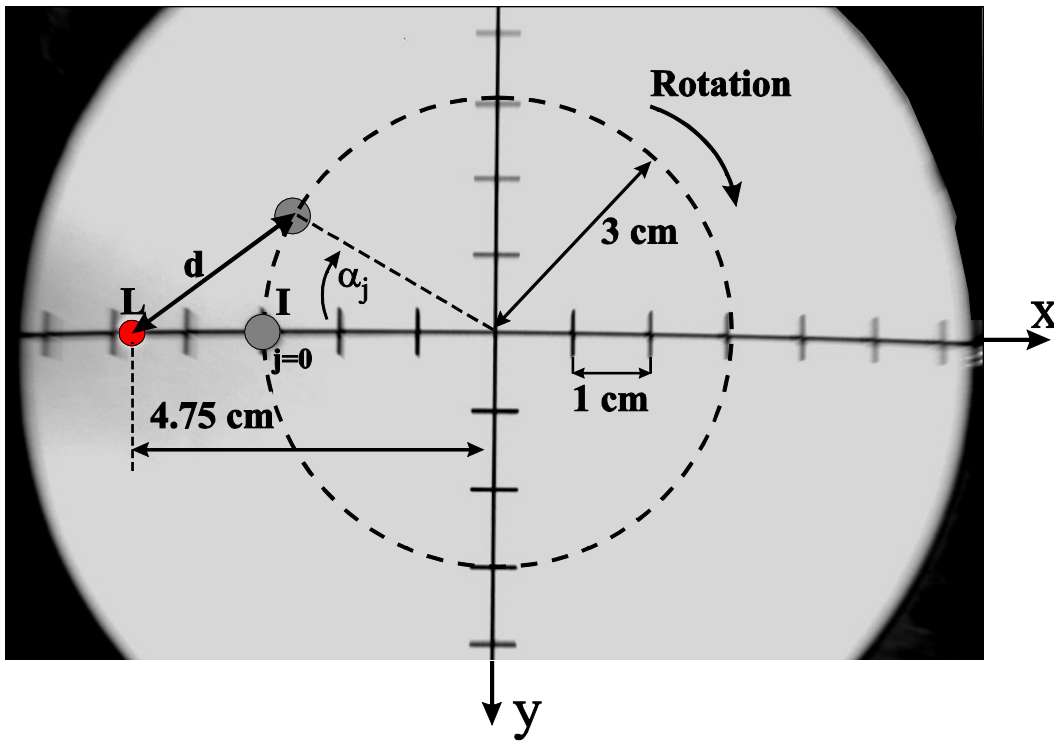"Wide field continuous wave reflectance optical topography including a clear layer on top of the diffusive surface."

Figure 2

N. A. Carbone, D. I. Iriarte and J. A. Pomarico.

"Wide field continuous wave reflectance optical topography including a clear layer on top of the diffusive surface."

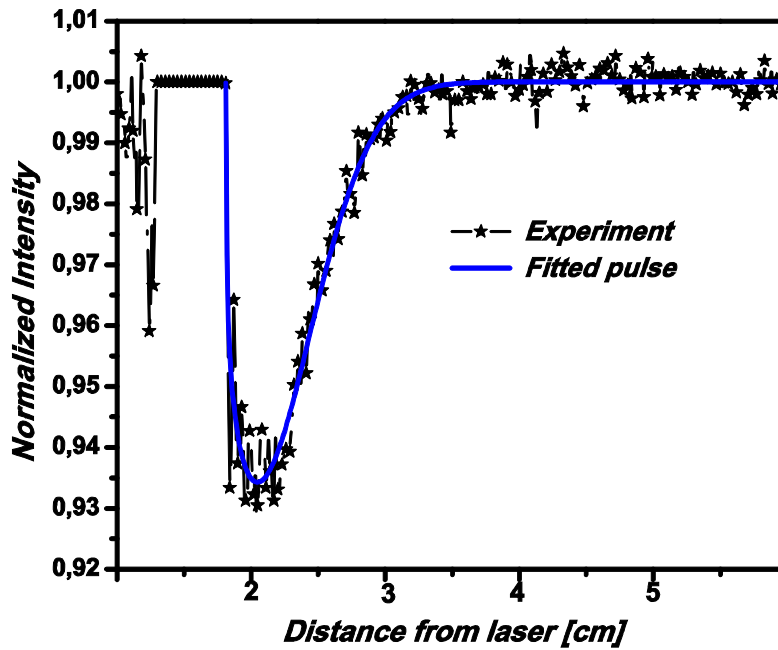**Figure 4**

N. A. Carbone, D. I. Iriarte and J. A. Pomarico.

"Wide field continuous wave reflectance optical topography including a clear layer on top of the diffusive surface."

15

Figure 5

N. A. Carbone, D. I. Iriarte and J. A. Pomarico.

"Wide field continuous wave reflectance optical topography including a clear layer on top of the diffusive surface."
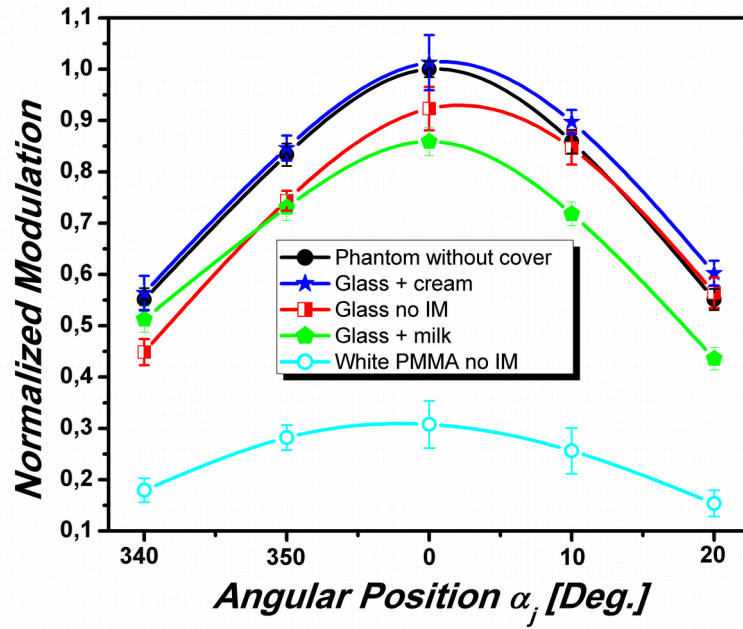
Figure 6

N. A. Carbone, D. I. Iriarte and J. A. Pomarico.

"Wide field continuous wave reflectance optical topography including a clear layer on top of the diffusive surface."

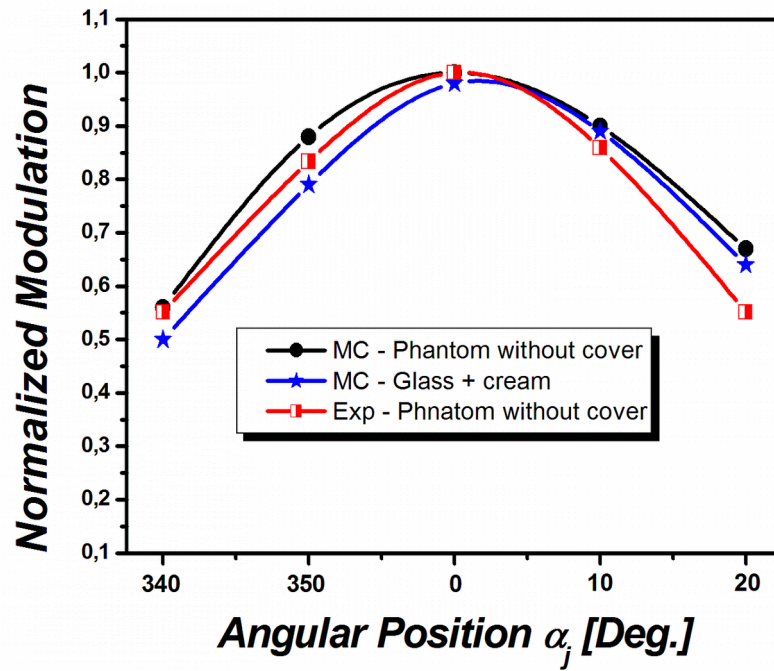**Table 1**

N. A. Carbone, D. I. Iriarte and J. A. Pomarico.

"Wide field continuous wave reflectance optical topography including a clear layer on top of the diffusive surface."

Position Phantom	Modulation [%] ±Relative error [%]				
	d^{340^0}	d^{350^0}	d^{0^0}	d^{10^0}	d^{20^0}
Phantom without Layer	4.26 ±0.17	6.50 ±0.17	7.80 ±0.12	6.70 ±0.18	4.30 ±0.16
Glass + Body Cream	4.40 ±0.26	6.60 ±0.19	7.90 ±0.42	7.40 ±0.18	4.70 ±0.19
Glass + Milk	4.00 ±0.20	5.70 ±0.20	6.70 ±0.21	5.60 ±0.18	3.40 ±0.17
Glas no IM	3.50 ±0.20	5.80 ±0.15	7.20 ±0.33	6.60 ±0.25	4.40 ±0.23
White PMMA no IM	1.40 ±0.18	2.20 ±0.19	2.40 ±0.36	2.20 ±0.35	1.20 ±0.20

Figure Captions

Figure 1: Schema of a patient lying decubito prono with the breast compressed against a flat transparent surface. The imaging system is placed under the stretcher.

Figure 2: Schema of the phantom used for the experiments showing the geometry for acquiring the images. The inclusion is an absorbing sphere placed at 3 cm from the center of the phantom and at 1.2 cm depth.

Figure 3: Photograph of the top surface of the phantom. The geometrical details are superimposed. L indicates the point at which the laser impinges and the spot labeled by I shows the inclusion at two angular positions.The phantom is rotated clockwise and for each angle α_j an image is acquired.

Figure 4: Experimental profile (line + symbols) corresponding to $\alpha_j = 10^0$ for the phantom covered with glass and using body cream as index matcher. The solid line is the fitting curve from which the modulation is calculated. Standard deviation of the data can be obtained from the fluctuations at distances far from the dip.

Figure 5: Plot of the normalized modulations for the different covering materials and index matching materials. Note that the glass cover with body cream as index matcher produces the same results as the phantom whitout cover. Other combinations produce lower modulations.

Figure 6: Plot of the normalized modulations obtained by Monte carlo simulations for the phantom without cover and for the glass cover with body cream as index matcher. The experimetal result for the phantom without cover is also shown for comparison purposes.

<u>Table captions:</u>

Table 1: Modulations obtained for the five distances from the illumination point and for all combinations between the interface material and index matchers.